International Journal of Heat and Mass Transfer 112 (2017) 509–520

Contents lists available at ScienceDirect

International Journal of Heat and Mass Transfer

journal homepage: www.elsevier.com/locate/ijhmt

Numerical simulation and sensitivity analysis of heat transfer enhancement in a flat heat exchanger tube with discrete inclined ribs

Nianben Zheng, Peng Liu, Zhichun Liu, Wei Liu *

School of Energy and Power Engineering, Huazhong University of Science and Technology, Wuhan 430074, China

ARTICLE INFO

Article history:
Received 20 December 2016
Received in revised form 17 April 2017
Accepted 5 May 2017
Available online 11 May 2017

Keywords:
Discrete inclined rib
Flat tube
Sensitivity analysis
Response surface methodology

ABSTRACT

In this work, we propose a numerical study of the thermal-hydraulic performance in a novel flat heat exchanger tube with discrete inclined ribs. Analysis of flow structures shows that four longitudinal swirl flows are induced in the flat tube. These swirl flows lead to adequate fluid mixing between the core flow and the near wall regions, and consequently, improve the heat transfer performance significantly. To determine the effects of parameters such as Reynolds number ($300 \leq Re \leq 1500$), the rib pitch ratio ($0.6 \leq P* \leq 1.8$), and the rib height ratio ($0.06 \leq H* \leq 0.18$) on the thermal and flow performance, a sensitivity analysis has been carried out by means of Response Surface Methodology. It is found that a reducing of $P*$ and an increase in $H*$ causes an increment in the Nusselt number and friction factor. The highest values of the Nusselt number and friction factor are achieved at $P* = 0.6$ and $H* = 0.18$ when Re is held at 900. Besides, the Nusselt number is more sensitive to Re and $H*$ while the friction factor is more sensitive to $P*$. The findings from this work may provide useful guidelines for engineers and researchers to design efficient heat exchangers.

1. Introduction

Heat exchangers, which make heat exchange possible between fluids, are widely used in various engineering applications such as air conditioning, refrigeration systems, solar collectors, and automotive radiators. To meet the ever-increasing thermal load and design compact heat exchangers for applications in the fields where space is strictly restricted, many researchers have proposed and investigated different enhanced heat transfer techniques during the past few years. The high surface area to the cross-sectional area ratio of flat tubes makes them superior to circular tubes in attempts to enhance the heat transfer rate and reduce the size of heat exchangers [1]. Hence, replacing circular tubes used in heat exchangers with flat tubes is an impressive technique for efficient heat exchangers.

In the field of using flat tubes, some investigations have been performed to further intensify their thermal performance. Ibrahim [2] experimentally explored the flow and heat transfer behaviors in a flat tube with helical screw-tape. Their results indicated that the flat tubes with helical screw-tapes further intensify the thermal performance of flat tubes. Safikhani and Abbassi [3] examined the combined use of nanofluid and twisted tape to increase the heat transfer rate in flat tubes. They concluded that the twisted tape performed better than nanofluid on heat transfer enhancement. Abdolbaqi et al. [4] experimentally determined the turbulent flow and heat transfer in flat tubes with counter-twisted tape and co-twisted tape. According to their results, both twisted tapes could improve the thermal performance of flat tubes, and the heat transfer performance for co-twisted tape was about 22.5% worse than that of counter-twisted tape. The application of nanofluids for heat transfer enhancement considering their superior thermal physical properties was the subject of investigation in several studies such as Vajjha et al. [5] determined the Al_2O_3 and CuO nanofluid flow and heat transfer in flat tubes of an automotive radiator by numerical simulation. The results showed an increase in particle volume concentration led to an enhancement in heat transfer coefficient and skin friction coefficient. Safikhani and Abbassi [6] presented the influence of tube flattening on the flow structures and thermal performance of nanofluids by numerical simulations. They found that both wall shear stress and heat transfer rate increased with the increment of tube flattening. Delavari et al. [7] numerically explored the nanofluid flow and heat transfer in flat tubes of a car radiator. Zhao et al. [8] evaluated the thermal performance of Al_2O_3–water nanofluids in a flat tube using entropy generation analysis. They found that tube flattening presented a more profound influence on the thermal performance than nanofluids. Multi-objective optimization of effective parameters

* Corresponding author.
E-mail address: w_liu@hust.edu.cn (W. Liu).

http://dx.doi.org/10.1016/j.ijheatmasstransfer.2017.05.019
0017-9310/

Nomenclature

a	width of a flat tube (mm)
ANOVA	analysis of variance
ANN	artificial neural network
b	height of a flat tube (mm)
b_0	the intercept
CFD	computational fluid dynamics
C_p	specific heat (J kg^{-1} K^{-1})
E	rib length (mm)
D_h	hydraulic diameter of a flat tube (mm)
f	friction factor
GA	genetic algorithm
H	rib height (mm)
h	heat transfer coefficient (W m^{-2} K^{-1})
$H*$	non-dimensional height ratio ($H* = H/D_h$)
k	thermal conductivity (W m^{-1} K^{-1})
L	length of a flat tube (mm)
Nu	Nusselt number
P	rib pitch (mm)
$P*$	non-dimensional pitch ratio ($P* = P/D_h$)
p	pressure (Pa)
q	heat flux (W m^{-2})
RSM	response surface methodology
R^2	coefficient of multiple determination
Re	Reynolds number
T	temperature (K)
U	velocity (m s^{-1})
W	rib width (mm)

Greek symbols

α	rib inclination angle (°)
ε	error
ρ	density (kg m^{-3})
μ	dynamic viscosity (kg m^{-1} s^{-1})

Subscripts

m	mean
w	wall

on nanofluids flow in flat tubes was carried out by Safikhani et al. [9] by computational fluid dynamics (CFD), artificial neural network (ANN), and genetic algorithm (GA).

Utilizing ribs or fins is another effective technique for heat transfer enhancement [10]. Sayed Ahmed et al. [11] conducted a comprehensive review on the flow and heat transfer characteristics in finned tube heat exchangers. Later, Sayed Ahmed and his coworkers [12,13] numerically examined and analyzed the influence of longitudinal fins on the thermal-hydraulic behavior for wing-shaped-tubes in cross-flow. Ghani et al. [14] applied the rectangular ribs and cavities to enhance the thermal performance in a microchannel heat sink. Staggered 45-deg ribs were proposed by Deng et al. [15] to increase the heat transfer performance in a rotating channel. The results indicated that heat transfer was enhanced by 40–80% with the use of the ribs. Yang et al. [16] experimentally determined the heat transfer and pressure drop behavior in a square channel with high blockage ribs. It was found that the thermal performance in the two-side ribbed channel was much higher than that in the one-side ribbed channel. Xie et al. [17] presented numerical simulations to study the turbulent heat transfer in a square channel with mid-truncated ribs. Their results showed that the 135° mid-truncated ribs provided the best heat transfer enhancement. Arc rib structures were introduced and examined in a channel by Wang et al. [18]. Chai et al. [19] numerically examined the thermal-hydraulic performance of laminar flow in a microchannel with offset ribs. The idea of discrete double-inclined ribs was, firstly, introduced based on heat transfer optimization by Meng [20]. It was found that multiple longitudinal vortexes were induced by the ribs. These unique flow structures were later visualized by Li et al. [21] with the aid of dying injection experiments. Wang et al. [22] analyzed the laminar heat transfer in a mini-channel with discrete double-inclined ribs. According to their results, ribs enhanced the thermal performance effectively. Zheng et al. [23] numerically explored the turbulent heat transfer performance in a tube with discrete inclined ribs and grooves based on the entropy generation analysis.

According to the literature survey, flat tubes and ribs are two effective techniques for heat transfer enhancement. However, the combined use of them has rarely been reported. The lack of information about this investigation has prompted the present work. In this paper, we propose the combined utilization of flat tubes and discrete inclined ribs to enhance the thermal-hydraulic performance. Numerical simulations and sensitivity analysis of parameters such as the Reynolds number, the rib pitch ratio, and the rib height ratio on the heat transfer and flow performance in the proposed flat tube have been performed by Response Surface Methodology (RSM), which has been proven very practical for solving thermal problems [24–35]. The findings from this work may provide convenient guidelines for engineers and researchers to design efficient heat exchangers.

2. Physical model

The physical model considered in this work is presented in Fig. 1. The flat tube is the same as the one in [8], which has a length (L) of 500 mm, a width (a) of 12.28 mm and height (b) of 6 mm. Also, the hydraulic diameter (D_h) of the flat tube is 8.4 mm. Discrete and inclined ribs are mounted on the two flat walls. The main geometric characteristics of these ribs are rib width (W), rib inclination angle (α), rib pitch (P), rib length (E) and rib height (H). In addition, the distance between the rib and the central axis of the flat tube is 1.17 mm, and the distance between the rib and the inlet of the flat tube is 3 mm. The non-dimensional rib pitch ratio ($P* = P/D_h$) and height ratio ($H* = H/D_h$) are fixed as the proportions of the rib pitch and rib height to the hydraulic diameter of the flat tube, respectively. More details about the geometric parameters of the flat tube and ribs are shown in Table 1.

3. Mathematical model

3.1. Governing equations

The commercial CFD software ANSYS Fluent 15.0 [36] has been applied to perform the numerical analysis. The flow and heat transfer phenomenon considered in this paper is assumed steady, laminar, and three-dimensional. During the numerical simulation, the properties of water are held constant, and the effects of gravity, bubbles, and viscous dissipation are not taken into consideration. Based on the above assumptions, the governing equations are given as follows.

$$\nabla \cdot \mathbf{u} = 0 \tag{1}$$

$$\rho(\mathbf{u} \cdot \nabla \mathbf{u}) = -\nabla p + \mu \nabla^2 \mathbf{u} \tag{2}$$

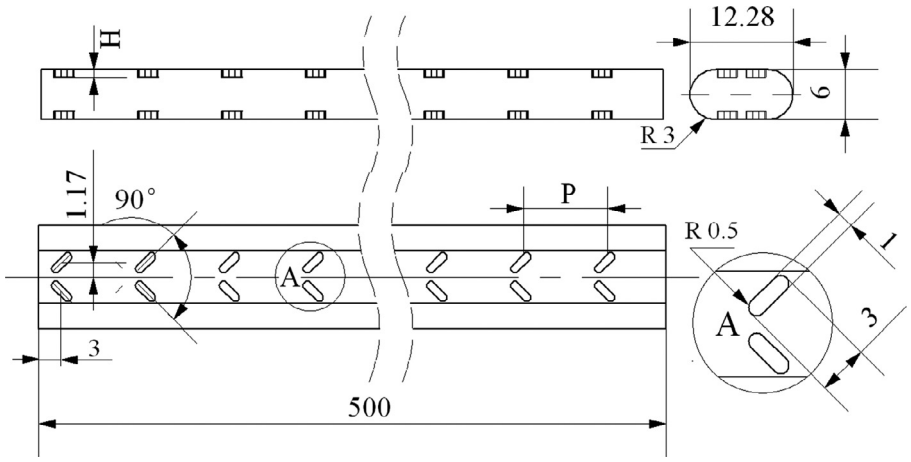

Fig. 1. Geometric characteristics of the flat tube and ribs (all dimensions except angle are in mm).

Table 1
Configuration parameters of the flat tube and ribs.

L/mm	a/mm	b/mm	D_h/mm	α/°	W/mm	E/mm	$P*$	$H*$
500	12.28	6	8.4	90	1	3	0.6–1.8	0.06–0.18

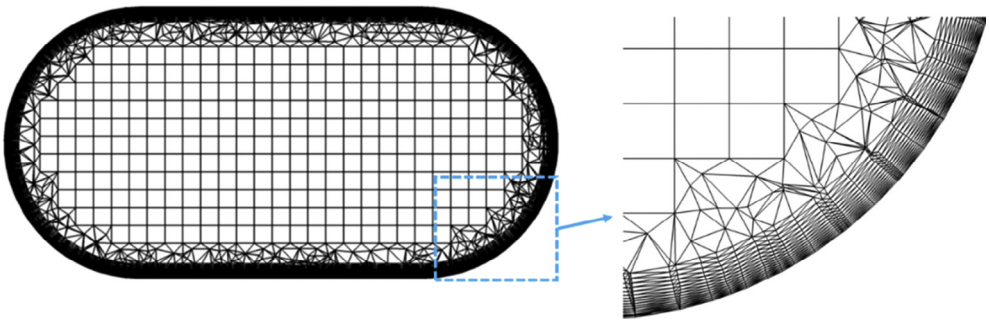

Fig. 2. Grid generation for the computational domain.

$$\rho C_p(\mathbf{u}\cdot\nabla T) = k(\nabla^2 T) \tag{3}$$

where k, μ, ρ, C_p are the thermal conductivity (W m^{-1} K^{-1}), dynamic viscosity (kg m^{-1} s^{-1}), density (kg m^{-3}), and specific heat (J kg^{-1} K^{-1}) of the working fluid (i.e., water), respectively. Also, T represents the temperature (K); p is the static pressure (Pa), and $\mathbf{u}$ represents the velocity vector (m s^{-1}).

As we know, the fully developed flow is preferred for investigation. However, the entry length for a heated tube is very long in laminar flow, and the physical length of a flat tube is usually not long enough that the flow in the flat tube is not fully developed in practical applications. To provide guidelines for practical applications, we investigate the flow and heat transfer behavior in the entrance region of the flat tube with discrete inclined ribs. It is worth noting that the flow in the smooth flat tube, which is considered as the reference for comparison, is also in the entrance region.

The uniform velocity and constant temperature (T_{in} = 273 K) are specified at the inlet. At the outlet a pressure-outlet condition (p_{out} = 0 Pa, gauge pressure) is set up. A constant and uniform heat flux of 2000 W m^{-2} and no-slip velocity condition are assigned to the surface of tube walls and ribs.

The average heat transfer coefficient (h) is defined as:

$$h = \frac{q}{T_w - T_m} \tag{4}$$

where T_w and T_m are the wall temperature (K) and the bulk temperature (K) of water, respectively, and q is the average heat flux (W m^{-2}).

The Nusselt number (Nu) is expressed as:

$$Nu = \frac{hD_h}{k} \tag{5}$$

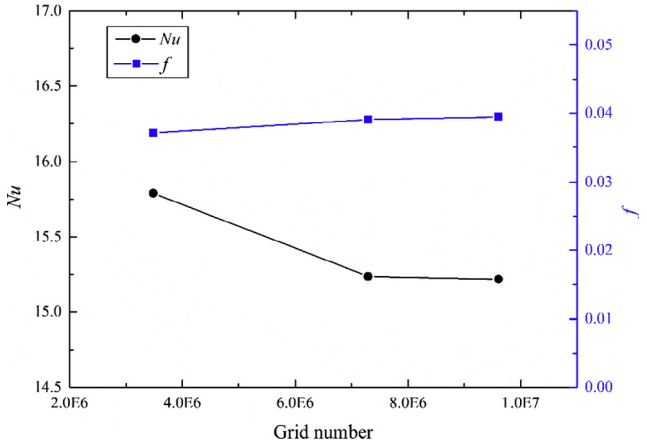

Fig. 3. Grid independence test.

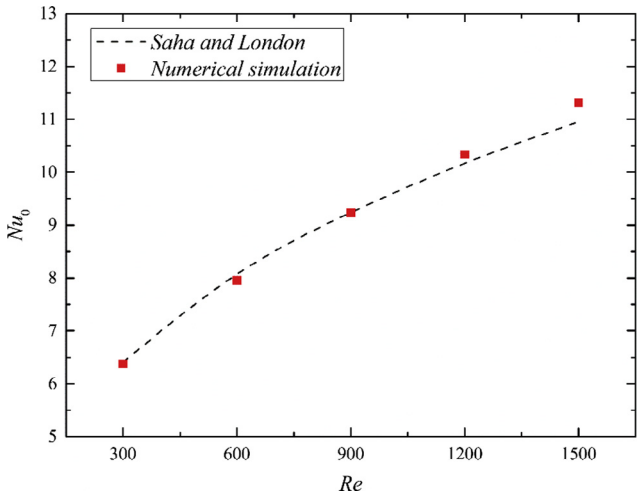

Fig. 4. Comparison of *Nu* between numerical results and theoretical formula from Saha and London [37].

Table 2
Design variables and their levels.

Variable	Level		
	−1	0	1
Re	300	900	1500
P∗	0.6	1.2	1.8
H∗	0.06	0.12	0.18

The friction factor (f) is defined as:

$$f = \frac{\Delta p}{(L/D_h)\rho U^2/2} \tag{6}$$

where Δp represents the pressure drop across the computational domain (Pa) and U is mean velocity (m s^{-1}) in the flat tube.

The definition of Reynolds number (Re) is given by:

$$Re = \frac{\rho U D_h}{\mu} \tag{7}$$

3.2. Numerical methods

During the simulation, the double precision solver is selected for precise results. To discretize the pressure term, the standard scheme is applied. To discretize the momentum and energy terms, the second-order upwind scheme is utilized. The well-known SIMPLE algorithm is used to handle the coupling between the pressure and velocity field. The solution is considered to be converged when all the residues are less than a prescribed value of 10^{-6}.

3.3. Grid generation and model validation

To implement the finite volume method, the computational domain should be discretized at first. Herein we use GAMBIT 2.4.6 to generate the non-uniform hybrid grids considering the complexity of the regions near the ribs. As shown in Fig. 2, the regions near the ribs and the tube wall were meshed with prism grids, and the core flow region was meshed with fine hexahedral elements. To fill the area between the wall and the core flow region, tetrahedral elements were finally employed. Besides, all the meshes were smoothed to improve their quality before exporting for calculation.

To make sure that the results of calculation are independent of the grid number, a rigorous grid independence test should be done. Herein three sets of grid systems which are 3.48 million (coarse), 7.30 million (fine) and 9.61 million (finest) were used to perform the grid independence test. Fig. 3 shows the variation of *Nu* and *f* with grid number for the flat tube with discrete inclined ribs with $P* = 1.8$ and $H* = 0.06$ at $Re = 900$. It can be found from the figure that the differences between the values decrease with the increasing grid number. Quantitatively, the differences between the coarse grid and the fine grid are 0.5549 for *Nu* and 0.0020 for *f*, and the differences between the fine grid and the finest grid are 0.0183 for *Nu* and 0.0004 for *f*. Besides, the relative errors between the fine grid and the finest grid are 0.12% for *Nu* and 1% for *f*, which implies that the fine grid system with 7.30 million elements ensures the accuracy of numerical simulations. Therefore, the similar grid system is employed in the following simulations.

To further ensure the accuracy of the present numerical simulation, the calculated results were compared with the theoretical results of Saha and London [37]. Results of comparison have been illustrated in Fig. 4. A good agreement between the present numerical results and the theoretical results is observed, and the maximum relative error is within 3.3%, indicating the current numerical method is reliable.

Table 3
Design of experiments.

Run order	Coded value			Real value			Response	
	Re	*P*∗	*H*∗	*Re*	*P*∗	*H*∗	*Nu*	*f*
1	0	0	−1	900	1.2	0.06	17.29	0.0446
2	1	1	−1	1500	1.8	0.06	21.42	0.0318
3	1	1	1	1500	1.8	0.18	34.18	0.0758
4	−1	0	0	300	1.2	0.12	12.19	0.1090
5	−1	1	1	300	1.8	0.18	13.07	0.1292
6	0	0	0	900	1.2	0.12	24.93	0.0788
7	0	0	1	900	1.2	0.18	31.75	0.1171
8	0	0	0	900	1.2	0.12	24.93	0.0788
9	0	−1	0	900	0.6	0.12	36.14	0.1326
10	0	1	0	900	1.8	0.12	20.71	0.0628
11	−1	1	−1	300	1.8	0.06	7.47	0.0694
12	−1	−1	1	300	0.6	0.18	20.39	0.2420
13	1	0	0	1500	1.2	0.12	34.37	0.0668
14	−1	−1	−1	300	0.6	0.06	9.86	0.0831
15	1	−1	−1	1500	0.6	0.06	31.14	0.0554
16	0	0	0	900	1.2	0.12	24.93	0.0788
17	0	0	0	900	1.2	0.12	24.93	0.0788
18	0	0	0	900	1.2	0.12	24.93	0.0788
19	1	−1	1	1500	0.6	0.18	54.77	0.1579
20	0	0	0	900	1.2	0.12	24.93	0.0788

4. Response surface methodology (RSM)

In order to investigate the influence of the three input parameters, i. e., *Re*, $P*$, and $H*$ on the *Nu* and *f* in the proposed flat tube, the statistic Response Surface Methodology (RSM) is adopted. According to Montgomery [38], RSM is one of the practical techniques for modeling multivariate problems in which the responses of interest are affected by input variables simultaneously. In most RSM problems, the first job is to determine an adaptive approximation for the functional relationship between the output and input variables (design parameters) by experiments and analysis. There are many RSM models available. Usually, the second-order RSM model considering the entire linear, square, and interaction terms is adequate to approximate the response. The second-order or quadratic polynomial model is given by:

$$y = b_0 + \sum_{i=1}^{k} b_i x_i + \sum_{i=1}^{k} b_{ii} x_i^2 + \sum\sum_{i<j} b_{ij} x_i x_j + \varepsilon \quad (8)$$

where b_0 represents the intercept; b_i, b_{ii}, b_{ij} represent the linear, square and interaction regression coefficients, respectively. x_i and x_j are the independent input variables, and y accounts for the response variable.

To fit the second-order model, a central composite design (CCD) which was originally proposed by Box and Wilson [39] is employed. Now it is the most popular class of designs for fitting the second-order models. The CCD for present work contains 20 runs for three input variables, each at three levels, as summarized in Table 2. The values of (−1), (0), (1) mean the low, middle and high levels of the variable, respectively. Arrangements of the runs of simulation regarding both coded values and real values based on the CCD are shown in Table 3. After finishing the runs of numerical simulation, the obtained *Nu* and *f* are then utilized to find the coefficients of the quadratic polynomial equation using the analytical software.

5. Results and discussion

5.1. Analysis of the flow and temperature fields

Before analyzing the influence of parameters on the *Nu* and *f* in the proposed flat tube, there is a need to understand the flow and temperature fields in the tube. Fig. 5(a) presents the local streamlines around the ribs. It is apparent from the figure that strong vortexes are induced right behind the ribs due to the disturbance of ribs. These vortexes result in flow deviation from the mainstream that the fluid within the core flow region tends to flow towards the near wall regions. The effect of vortexes on the local temperature distributions is illustrated in Fig. 5(b). From the contours of local temperature, we can see that the temperature in the front areas of the ribs is much lower than that in the other regions because of the direct impingement of the fluid. The temperature in the areas right behind the ribs where vortexes are generated is the highest indicating the heat transfer performance is poor in these areas. It is noted that the temperature in the area far away from the back of ribs tends to decrease, implying an improvement in heat transfer performance, which can be attributed to the flow deviation caused by vortexes.

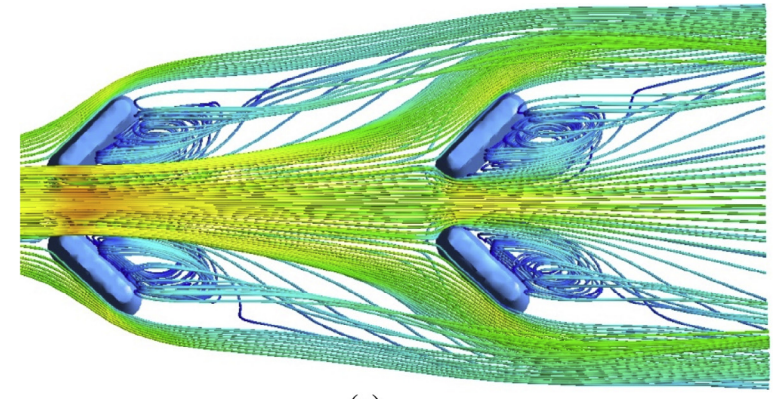

(a)

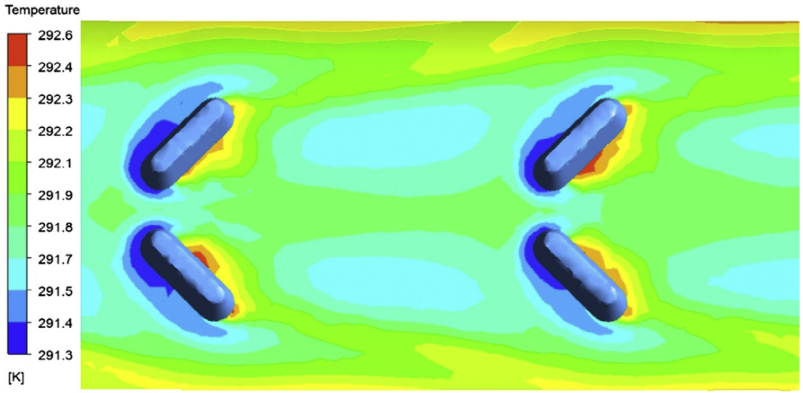

(b)

Fig. 5. Local streamlines and temperature distributions around the ribs: (a) three-dimensional streamline; (b) temperature.

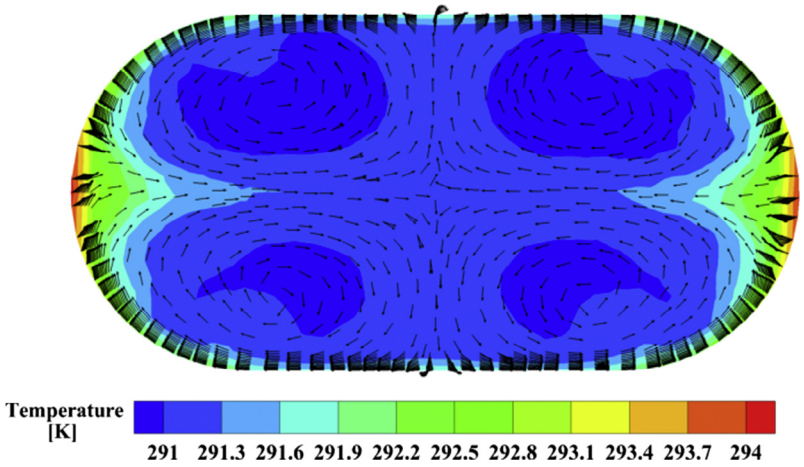

Fig. 6. Temperature and velocity vectors at the outlet of the flat tube.

The contours of temperature with superimposed velocity vectors at the outlet of the ribbed tube are displayed in Fig. 6. One sees from the figure that four longitudinal swirl flows are induced by ribs. The notable function of these longitudinal swirl flows is that cold fluid within the core flow region can be fully mixed with the hot fluid near the heated wall, which improves the heat transfer performance significantly.

5.2. Analysis of variance and model estimation

The calculated *Nu* and *f* for the determined conditions are presented in Table 3. These responses are utilized for regression modeling, and the regression coefficients are tested for significance. The results of the statistical significance test for *Nu* and *f* are shown in Table 4 and 5, respectively.

Table 4
The results of analysis of variance for *Nu*.

Source	*DOF*	*Seq. SS*	*Adj. SS*	*Adj. MS*	*F-value*	*P-value*
Regression	9	2199.71	2199.71	244.412	126.47	0
Linear	3	2030.92	129.97	43.324	22.42	0
Re	1	1274.59	81.4	81.397	42.12	0
P∗	1	307.67	10.36	10.355	5.36	0.043
H∗	1	448.66	21.02	21.02	10.88	0.008
Square	3	33.27	33.27	11.091	5.74	0.015
ReRe	1	13.76	17.13	17.134	8.87	0.014
P∗P∗	1	15.19	19.3	19.298	9.99	0.01
H∗H∗	1	4.32	4.32	4.32	2.24	0.166
Interaction	3	135.52	135.52	45.173	23.37	0
ReP∗	1	53.04	53.04	53.043	27.45	0
ReH∗	1	51.25	51.25	51.249	26.52	0
P∗H∗	1	31.23	31.23	31.229	16.16	0.002
Residual error	10	19.33	19.33	1.933	–	–
Lack-of-fit	5	19.33	19.33	3.865	–	–
Pure error	5	0	0	0	–	–
Total	19	2219.04	–	–	–	–

R^2 = 99.13%, R^2 (Predicted) = 90.54%, R^2 (Adjusted) = 98.35%

Table 5
The results of analysis of variance for *f*.

Source	*DOF*	*Seq. SS*	*Adj. SS*	*Adj. MS*	*F-value*	*P-value*
Regression	9	0.040976	0.040976	0.004553	104.5	0
Linear	3	0.034306	0.001797	0.000599	13.75	0.001
Re	1	0.006002	0.000287	0.000287	6.58	0.028
P∗	1	0.009117	0.000638	0.000638	14.65	0.003
H∗	1	0.019186	0.001301	0.001301	29.87	0
Square	3	0.002853	0.002853	0.000951	21.83	0
ReRe	1	0.001814	0.000173	0.000173	3.96	0.075
P∗P∗	1	0.001037	0.00086	0.00086	19.74	0.001
H∗H∗	1	0.000002	0.000002	0.000002	0.05	0.834
Interaction	3	0.003818	0.003818	0.001273	29.21	0
ReP∗	1	0.000054	0.000054	0.000054	1.25	0.29
ReH∗	1	0.000654	0.000654	0.000654	15	0.003
P∗H∗	1	0.00311	0.00311	0.00311	71.38	0
Residual error	10	0.000436	0.000436	0.000044	–	–
Lack-of-fit	5	0.000436	0.000436	0.000087	–	–
Pure error	5	0	0	0	–	–
Total	19	0.041412	–	–	–	–

R^2 = 98.95%, R^2 (Predicted) = 84.12%, R^2 (Adjusted) = 98.00%

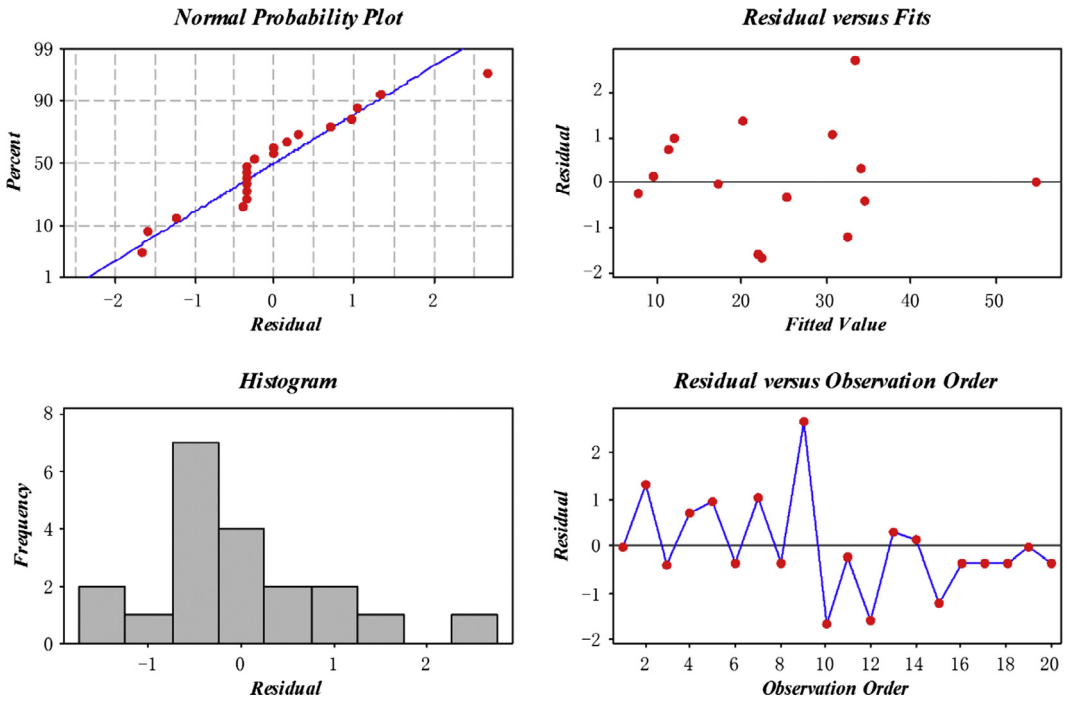

Fig. 7. Residual plots of the Nusselt number.

In Table 4 and 5, the degree of freedom (*DOF*) is equal to the number of levels of the variable minus one. The total sum of squares (*SS*) helps express the total variation attributed to various factors, and *Seq. SS* means the sequential sums of squares, and *Adj. SS* represents the adjusted sums of squares. The mean square (*MS*) is the sum of squares divided by the degrees of freedom. The *F-value* is a ratio of mean squares, and a higher *F-value* indicates a more significant effect. The *P-value* means a probability that determines the evidence against the null hypothesis, and a lower *P-value* provides a stronger evidence against the null hypothesis. Besides, R^2 is the coefficient of determination or multiple determination. Usually, a higher R^2 means that the model fits the data better. R^2 (Predicted) is used to determine how well the model predicts responses for new observations, and R^2 (Adjusted) means the adjusted coefficient of determination. More details about statistical estimators for analysis of variance are available in [40].

According to Table 4, the R^2 value for the model is 99.13%, which intends that only 0.87% of total change cannot be embodied by the model. The R^2 (Predicted) and R^2 (Adjusted) are also provided, which present the high accuracy of the RSM model. Furthermore, the *F-value* of this model is equal to 126.47, which is much larger than unity, indicating that the present regression model is significant. Therefore, the present model shows high accuracy for the calculation of the Nusselt number. In addition, to determine whether the model terms are significant or not, analysis has been conducted based on the *P-value*, with 95% certainty. In other words, the terms with *P-value* less than 0.05 are significant for the model and the terms with *P-value* larger than 0.05 are meaningless, which should be rejected.

In this case, it is can be concluded from Table 4 that the linear terms of the *Re*, *P*∗ and *H*∗, the square terms of *ReRe* and *P*∗*P*∗, together with the interaction terms of *ReP*∗, *ReH*∗ and *R*∗*H*∗ are the meaningful terms related to the Nusselt number, while the square term of *H*∗*H*∗ presents a meaningless influence. Besides, the sensitivity level of the mentioned meaningful terms for the Nusselt number from low to high is the square term, the linear term, and the interaction term. Moreover, among the factors affecting the Nusselt number, the linear term of *Re* is the most significant one.

According to Table 5, the R^2 value for the model is 98.95%, suggesting that only 1.07% of total change cannot be embodied by the model. Also, the R^2 (Predicted) and R^2 (Adjusted) are provided, which indicate the high accuracy of the RSM model. The high *F-value* of 104.5 implies that the present regression model is significant. According to the *P-value* with 95% certainty, the meaningful model terms related to the friction factor are the linear terms of the *Re*, *P*∗ and *H*∗, the square term of *P*∗*P*∗, and the interaction terms of *ReH*∗ and *P*∗*H*∗. However, the effects of the square terms of *ReRe* and *H*∗*H*∗ and the interaction term of *ReP*∗ are insignificant. It is worth noting that the sensitivity level of the mentioned significant model terms for the friction factor from high to low is the interaction term, the square term, and the linear term, and the interaction term of *P*∗*H*∗ is the most significant for the friction factor.

To further validate the RSM model and obtain the estimated regression, the residual plots, which are graphs applied to examine the goodness-of-fit in regression for *Nu* and *f* achieved by the analysis of variance, have been presented in Fig. 7 and 8, respectively. The residual plots include the normal probability plot of residuals, histogram of the residuals, residuals versus fits and residuals versus order of data. To examine the normality of the observation, the normal probability plots of residual distributions are displayed in Figs. 7 and 8. We can see that the diagrams of normal probability are straight lines, which imply that the residual distributions for both *Nu* and *f* are normal. To determine whether the data are skewed or whether outliers exist in the data, the histogram of the residuals are presented. It is evident the residual histograms have skewed distributions, but as a whole, they approach to a symmetrical distribution. From the residuals versus fits plots in Figs. 7 and 8, one sees that the maximum residuals are within 2.68 and 0.008 for *Nu* and *f*, respectively, and the residuals roughly form a horizontal band around the zero line, implying that the variances of the error terms are equal. Besides, it is notable that all the residuals are within the basic random pattern of residuals, which

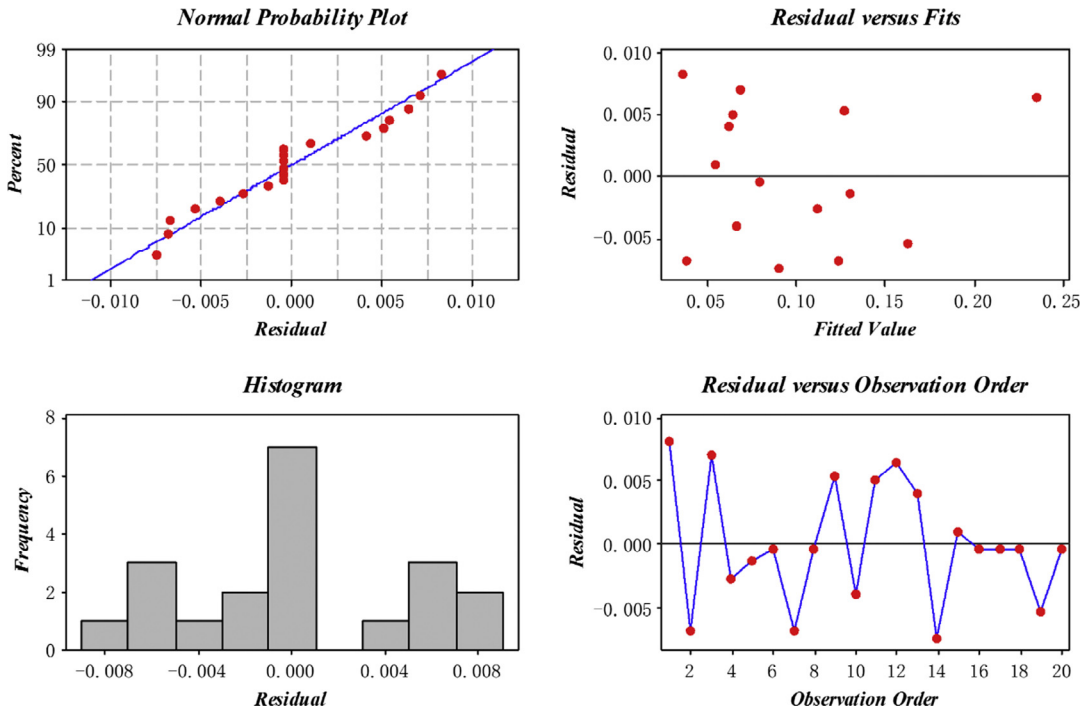

Fig. 8. Residual plots of the friction factor.

suggests that there are no outliers. The residuals versus order plots for *Nu* and *f* are also presented in Figs. 7 and 8. It is clear that the residuals for *Nu* and *f* bounce randomly around the zero line, suggesting that the residuals are uncorrelated with each other. Therefore, it can be concluded that the present RSM model has reasonable accuracy.

The general models obtained by Response Surface Methodology for evaluating the relationship between the responses (*Nu* and *f*) and effective input parameters (*Re*, $P*$ and $H*$) can be expressed as follows:

$$Nu \text{ or } f = b_0 + b_1 Re + b_2 P^* + b_3 H^* + b_{11} ReRe + b_{22} P^* P^* + b_{33} H^* H^* + b_{12} ReP^* + b_{13} ReH^* + b_{23} P^* H^* \quad (9)$$

The estimated coefficients of Eq. (9) for *Nu* and *f*, which are obtained as coded units are displayed in Table 6. It is remarkable that the meaningless model terms are neglected, and only the significant terms are adopted. The specific functional relationships between responses and input variables are given by:

$$Nu = 25.265 + 11.290Re - 5.547P^* + 6.698H^* - 2.496ReRe + 2.649P^*P^* - 2.575ReP^* + 2.531ReH^* - 1.976P^*H^* \quad (10)$$

$$f = 0.0793 - 0.0245Re - 0.0302P^* + 0.0438H^* + 0.0177P^*P^* - 0.0090ReH^* - 0.0197P^*H^* \quad (11)$$

5.3. Response surface analysis

To investigate the effects of effective parameters on the *Nu* and *f*, both 2–D and 3–D response surface contour plots have been presented in Figs. 9 and 10.

Fig. 9(a)–(c) show the effects of *Re*–$P*$, *Re*–$H*$, $P*$–$H*$ on the response *Nu*, respectively. It can be seen from Fig. 9(a) that increasing in *Re* and decreasing $P*$ enhances the Nusselt number. The maximum Nusselt number is obtained at *Re* = 1500 and $P*$ = 0.6, and the minimum Nusselt number is observed at *Re* = 300 and $P*$ = 1.8. Fig. 9(b) indicates the variations of the Nusselt number with *Re* and $H*$. An enhancement in both *Re* and $H*$ results in an improvement in the Nusselt number. The highest value of the Nusselt number is obtained at *Re* = 1500 and $H*$ = 0.18, while the lowest value is observed at *Re* = 300 and $H*$ = 0.06. Variations of the Nusselt number with $P*$ and $H*$ are displayed in Fig. 9(c). One can see from the figure that reducing of $P*$ and an increase in $H*$ causes an increment in the Nusselt number. The maximum Nusselt number is achieved at $P*$ = 0.6 and $H*$ = 0.18, while the minimum value is observed at $P*$ = 1.8 and $H*$ = 0.06.

Table 6
Estimated regression coefficients of response surface models.

Coefficient	*Nu*	*f*
b_0	25.265	0.0793
b_1	11.290	−0.0245
b_2	−5.547	−0.0302
b_3	6.698	0.0438
b_{11}	−2.496	0
b_{22}	2.649	0.0177
b_{33}	0	0
b_{12}	−2.575	0
b_{13}	2.531	−0.0090
b_{23}	−1.976	−0.0197

Variations of the friction factor with *Re* and $P*$ are displayed in Fig. 10(a). The friction factor decreases with an increment in *Re* and $P*$, and its lowest value is achieved at *Re* = 1500 and $P*$ = 1.8 and its highest value at *Re* = 300 and $P*$ = 0.6. Fig. 10(b) presents the changes of the friction factor with *Re* and $H*$. A decrease in *Re* and an enhancement of $H*$ results in an increment in the friction factor. The maximum value is obtained at *Re* = 300 and $H*$ = 0.18 and the minimum value at *Re* = 1500 and $H*$ = 0.06. Fig. 10(c) presents the changes of the friction factor regarding $P*$ and $H*$ variations. It is obvious that reducing of $P*$ and increasing in $H*$ increases the friction factor, and its highest value is observed at $P*$ = 0.6 and $H*$ = 0.18 and its lowest value is obtained at $P*$ = 1.8 and $H*$ = 0.06.

6. Sensitivity analysis

Sensitivity analysis, which is a method to determine how the uncertainties in a model input affect the output of the model [41], is of great importance for numerical simulation. In the context of the present work, sensitivity analysis refers to determining the influence of the input parameters of the RSM model on the output variables. By the utilization of the results of sensitivity analysis, the effective parameters can be ranked in order of influence, and finally the most effective parameter can be specified.

Mathematically, the partial derivatives of the *Nu* and *f* respect to certain effective parameter are calculated as the sensitivity of

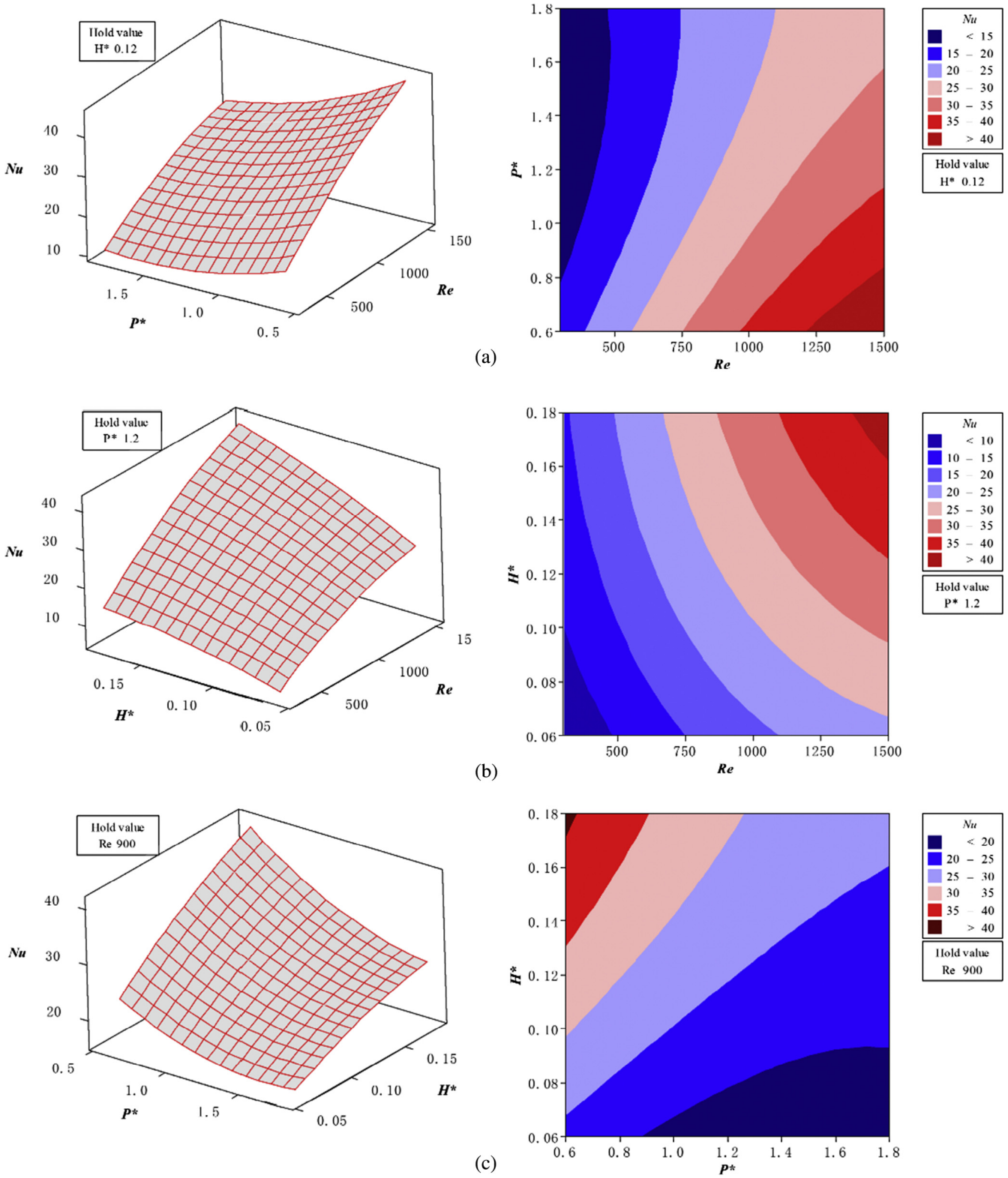

Fig. 9. Variations of *Nu* with effective parameters: (a) *Re*–*P*∗; (b) *Re*–*H*∗; (c) *P*∗–*H*∗.

the output variables respect to those effective parameters. Therefore, the partial derivatives of Eqs. (10) and (11) to input parameters are calculated, and they are given as follows:

$$\frac{\partial Nu}{\partial Re} = 11.290 - 4.892\frac{\partial f}{\partial Re} = -0.0245 - 0.0090H^{*}Re - 2.575P^{*} + 2.531H^{*} \quad (12)$$

$$\frac{\partial Nu}{\partial P^{*}} = -5.547 + 5.298P^{*} - 2.575Re - 1.976H^{*} \quad (13)$$

$$\frac{\partial Nu}{\partial H^{*}} = 6.698 + 2.531Re - 1.976P^{*} \quad (14)$$

$$\frac{\partial f}{\partial Re} = -0.0245 - 0.0090H^{*} \quad (15)$$

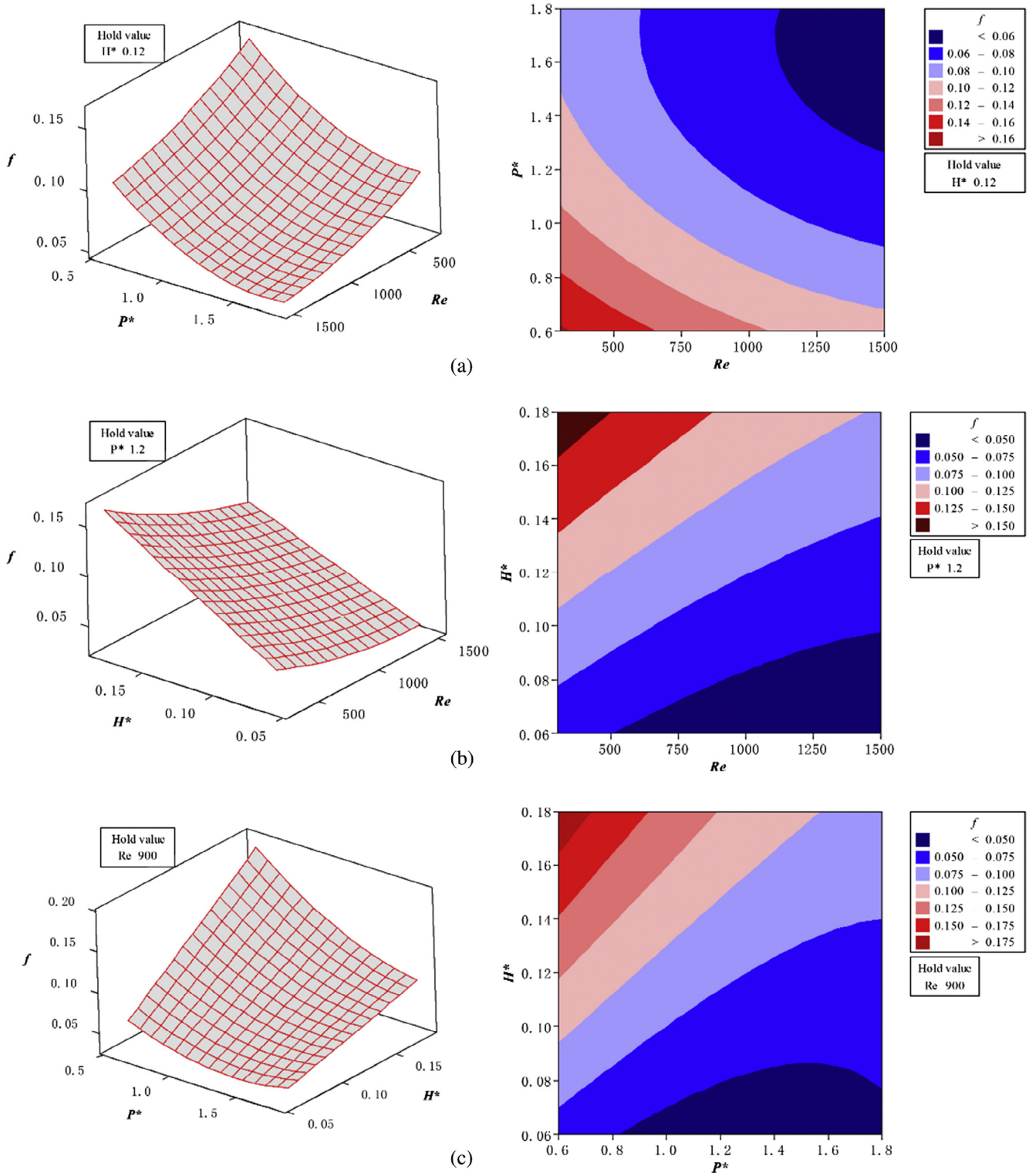

Fig. 10. Variations of f with effective parameters: (a) Re–$P*$; (b) Re–$H*$; (c) $P*$–$H*$.

Table 7
Sensitivity analysis of *Nu*.

Re	$P*$	$H*$	$\frac{\partial Nu}{\partial Re}$	$\frac{\partial Nu}{\partial P^*}$	$\frac{\partial Nu}{\partial H^*}$
−1	0	−1	13.751	−0.996	4.167
		0	16.282	−2.972	4.167
		1	18.813	−4.948	4.167
0		−1	8.759	−3.571	6.698
		0	11.290	−5.547	6.698
		1	13.821	−7.523	6.698
1		−1	3.766	−6.146	9.229
		0	6.297	−8.122	9.229
		1	8.829	−10.098	9.229
−1	1	−1	11.176	4.302	2.191
		0	13.707	2.326	2.191
		1	16.238	0.350	2.191
0		−1	6.184	1.727	4.722
		0	8.715	−0.249	4.722
		1	11.246	−2.225	4.722
1		−1	1.192	−0.848	7.253
		0	3.723	−2.824	7.253
		1	6.254	−4.799	7.253

Table 8
Sensitivity analysis of *f*.

Re	$P*$	$H*$	$\frac{\partial f}{\partial Re}$	$\frac{\partial f}{\partial P^*}$	$\frac{\partial f}{\partial H^*}$
−1	0	−1	−0.015	−0.010	0.053
		0	−0.024	−0.030	0.053
		1	−0.034	−0.050	0.053
0		−1	−0.015	−0.010	0.044
		0	−0.024	−0.030	0.044
		1	−0.034	−0.050	0.044
1		−1	−0.015	−0.010	0.035
		0	−0.024	−0.030	0.035
		1	−0.034	−0.050	0.035
−1	1	−1	−0.015	0.025	0.033
		0	−0.024	0.005	0.033
		1	−0.034	−0.015	0.033
0		−1	−0.015	0.025	0.024
		0	−0.024	0.005	0.024
		1	−0.034	−0.015	0.024
1		−1	−0.015	0.025	0.015
		0	−0.024	0.005	0.015
		1	−0.034	−0.015	0.015

$$\frac{\partial f}{\partial P^*} = -0.0302 + 0.0354P^* - 0.0197H^* \tag{16}$$

$$\frac{\partial f}{\partial H^*} = 0.0438 - 0.0090Re - 0.0197P^* \tag{17}$$

It is worth noting that a positive sensitivity value indicates an increase in input parameters leads to an increment in output parameter while a negative value implies the opposite trend. The results from this analysis obtained from Eqs. (12)(17) are presented in Table 7 and 8. These values in the tables are achieved in the proposed flat tube with *Re* at levels of −1, 0 and 1 (300, 900, 1500), $P*$ at levels of 0 and 1 (1.2 and 1.8) and $H*$ at levels of −1, 0 and 1 (0.06, 0.12 and 0.18). It should be noted that the parameter levels are selected based on the principle that the ranges of the parameters are wide enough to reflect the basic rules and characteristics of the sensitivity of *Nu* and *f* to effective input parameters.

Tables 7 and 8 show the sensitivity of *Nu* and *f* to effective input parameters, respectively. According to Table 7, it can be concluded that:

- The sensitivity of the Nusselt number to *Re* is positive. This positive sensitivity indicates that Nusselt number increases by increasing *Re*. Additionally, this sensitivity increases with an increment in $H*$.
- The sensitivity of the Nusselt number to $H*$ is positive and independent of $H*$. This positive sensitivity means that an increase in $H*$ causes an enhancement in the Nusselt number. Also, this sensitivity increases with increasing *Re*.
- The sensitivity of the Nusselt number to $P*$ is positive for high levels of $P*$ (1) and low levels of *Re* (−1). However, this sensitivity changes to negative at other values of $P*$ and *Re* and decreases with increasing $H*$.
- Comparison of the sensitivity shows that the Nusselt number is more sensitive to *Re* and $H*$. Therefore, researchers should pay more attention to the two parameters to design a flat heat exchanger tube for possible heat transfer enhancement.

Considering the results in Table 8, the following conclusions can be made:

- The sensitivity of the friction factor to *Re* is negative and independent of *Re* and $P*$. As a result, the friction factor decreases as *Re* increases. Additionally, an enhancement in $H*$ leads to a reduction in this sensitivity.
- The sensitivity of the friction factor to $H*$ is positive and independent of $H*$. The positive sensitivity means that an increment in the friction factor is observed with an enhancement in $H*$. Besides, this sensitivity decreases with the increment of *Re* and $P*$.
- The sensitivity of the friction factor to $P*$ is negative at low levels of $P*$ (0) and independent of *Re*. At high levels of $P*$ (1), this sensitivity is positive at low levels of $H*$ (−1 and 0) and changes to negative at high levels of $H*$ (1).
- Comparison of the sensitivity shows that the friction factor is more sensitive to the parameter $H*$. Therefore, researchers should notice to $H*$ to design a flat heat exchanger tube with the objective of reducing the pressure drop.
- The sensitivity of the friction factor to *Re*, $P*$ and $H*$ is less than the sensitivity of the Nusselt number to these parameters.

7. Conclusions

Numerical simulations and sensitivity analysis have been performed to investigate the combined use of flat tubes and discrete inclined ribs to enhance the thermal-hydraulic performance using Response Surface Methodology. The effects of three effective parameters including *Re* ($300 \le Re \le 1500$), $P*$ ($0.6 \le P* \le 1.8$) and $H*$ ($0.06 \le H* \le 0.18$) on the *Nu* and *f* are investigated and analyzed statistically. Based on the results of the numerical investigation and statistical analysis, the main findings from this work are summarized as follows:

(1) Four longitudinal swirl flows are induced by ribs. The notable function of these longitudinal swirl flows is that cold fluid within the core flow region can be fully mixed with the hot fluid near the heated wall, which improves the heat transfer performance significantly.
(2) Analysis of variance shows that the most significant terms for *Nu* and *f* are the linear term of *Re* and the interaction term of $P*H*$, respectively.
(3) A reducing of $P*$ and an increase in $H*$ causes an increase in *Nu* and *f*. The highest values of *Nu* and *f* are achieved at $P* = 0.6$ and $H* = 0.18$ when *Re* is held at 900.
(4) Among the effective input parameters, *Nu* is more sensitive to *Re* and $H*$ while *f* is more sensitive to the parameter $H*$.
(5) The sensitivity of *f* to *Re*, $P*$ and $H*$ is less than the sensitivity of *Nu* to these parameters.

Acknowledgments

The work was supported by the National Key Basic Research Program of China (973 Program) (2013CB228302) and the National Natural Science Foundation of China (51376069).

References

[1] P. Razi, M. Akhavan-Behabadi, M. Saeedinia, Pressure drop and thermal characteristics of CuO–base oil nanofluid laminar flow in flattened tubes under constant heat flux, Int. Commun. Heat Mass Transfer 38 (7) (2011) 964–971.
[2] E. Ibrahim, Augmentation of laminar flow and heat transfer in flat tubes by means of helical screw-tape inserts, Energy Convers. Manage. 52 (1) (2011) 250–257.
[3] H. Safikhani, F. Abbasi, Numerical study of nanofluid flow in flat tubes fitted with multiple twisted tapes, Adv. Powder Technol. 26 (6) (2015) 1609–1617.
[4] M.K. Abdolbaqi, W.H. Azmi, R. Mamat, N.M.Z.N. Mohamed, G. Najafi, Experimental investigation of turbulent heat transfer by counter and co-swirling flow in a flat tube fitted with twin twisted tapes, Int. Commun. Heat Mass Transfer 75 (2016) 295–302.
[5] R.S. Vajjha, D.K. Das, P.K. Namburu, Numerical study of fluid dynamic and heat transfer performance of Al_2O_3 and CuO nanofluids in the flat tubes of a radiator, Int. J. Heat Fluid Flow 31 (4) (2010) 613–621.
[6] H. Safikhani, A. Abbassi, Effects of tube flattening on the fluid dynamic and heat transfer performance of nanofluids, Adv. Powder Technol. 25 (3) (2014) 1132–1141.
[7] V. Delavari, S.H. Hashemabadi, CFD simulation of heat transfer enhancement of Al_2O_3/water and Al_2O_3/ethylene glycol nanofluids in a car radiator, Appl. Therm. Eng. 73 (1) (2014) 380–390.
[8] N. Zhao, J. Yang, H. Li, Z. Zhang, S. Li, Numerical investigations of laminar heat transfer and flow performance of Al_2O_3–water nanofluids in a flat tube, Int. J. Heat Mass Transfer 92 (2016) 268–282.
[9] H. Safikhani, A. Abbassi, A. Khalkhali, M. Kalteh, Multi-objective optimization of nanofluid flow in flat tubes using CFD, artificial neural networks and genetic algorithms, Adv. Powder Technol. 25 (5) (2014) 1608–1617.
[10] A. Kumar, M.H. Kim, Thermohydraulic performance of rectangular ducts with different multiple V-rib roughness shapes: a comprehensive review and comparative study, Renew. Sustain. Energy Rev. 54 (2016) 635–652.
[11] S.A.E. Sayed Ahmed, O.M. Mesalhy, M.A. Abdelatief, Flow and heat transfer enhancement in tube heat exchangers, Heat Mass Transfer 51 (11) (2015) 1607–1630.
[12] S.A.E. Sayed Ahmed, O.M. Mesalhy, M.A. Abdelatief, Effect of longitudinal-external-fins on fluid flow characteristics for wing-shaped tubes bundle in crossflow, J. Thermodyn. 2015 (2015).
[13] S.A.E. Sayed Ahmed, O.M. Mesalhy, M.A. Abdelatief, Heat transfer characteristics and entropy generation for wing-shaped-tubes with longitudinal external fins in cross-flow, J. Mech. Sci. Technol. 30 (6) (2016) 2849–2863.
[14] I.A. Ghani, N. Kamaruzaman, N.A.C. Sidik, Heat transfer augmentation in a microchannel heat sink with sinusoidal cavities and rectangular ribs, Int. J. Heat Mass Transfer, Part B 108 (2017) 1969–1981.
[15] H. Deng, Y. Li, Z. Tao, G. Xu, S. Tian, Pressure drop and heat transfer performance in a rotating two-pass channel with staggered 45-deg ribs, Int. J. Heat Mass Transfer, Part B 108 (2017) 2273–2282.
[16] W. Yang, S. Xue, Y. He, W. Li, Experimental study on the heat transfer characteristics of high blockage ribs channel, Exp. Thermal Fluid Sci. 83 (2017) 248–259.
[17] G. Xie, J. Liu, P.M. Ligrani, B. Sunden, Flow structure and heat transfer in a square passage with offset mid-truncated ribs, Int. J. Heat Mass Transfer 71 (2014) 44–56.
[18] H.T. Wang, W.B. Lee, J. Chan, S. To, Numerical and experimental analysis of heat transfer in turbulent flow channels with two-dimensional ribs, Appl. Therm. Eng. 75 (2015) 623–634.
[19] L. Chai, G.D. Xia, H.S. Wang, Numerical study of laminar flow and heat transfer in microchannel heat sink with offset ribs on sidewalls, Appl. Therm. Eng. 92 (2016) 32–41.
[20] J. Meng, Enhanced Heat Transfer Technology of Longitudinal Vortices Based on Field-Coordination Principle and Its Application, Power Engineering and Engineering Thermophysics, Tsinghua University, Beijing, 2003 (in Chinese).
[21] X. Li, H. Yan, J. Meng, Z. Li, Visualization of longitudinal vortex flow in an enhanced heat transfer tube, Exp. Thermal Fluid Sci. 31 (6) (2007) 601–608.
[22] Y. Wang, B. Zhou, Z. Liu, Z. Tu, W. Liu, Numerical study and performance analyses of the mini-channel with discrete double-inclined ribs, Int. J. Heat Mass Transfer 78 (2014) 498–505.
[23] N. Zheng, P. Liu, F. Shan, Z. Liu, W. Liu, Numerical investigations of the thermal-hydraulic performance in a rib-grooved heat exchanger tube based on entropy generation analysis, Appl. Therm. Eng. 99 (2016) 1071–1085.
[24] S. Mirzakhanlari, K. Milani Shirvan, M. Mamourian, A.J. Chamkha, Increment of mixed convection heat transfer and decrement of drag coefficient in a lid-driven nanofluid-filled cavity with a conductive rotating circular cylinder at different horizontal locations: a sensitivity analysis, Powder Technol. 305 (2017) 495–508.
[25] K. Milani Shirvan, M. Mamourian, S. Mirzakhanlari, R. Ellahi, K. Vafai, Numerical investigation and sensitivity analysis of effective parameters on combined heat transfer performance in a porous solar cavity receiver by response surface methodology, Int. J. Heat Mass Transfer 105 (2017) 811–825.
[26] K. Milani Shirvan, M. Mamourian, S. Mirzakhanlari, H.F. Öztop, N. Abu-Hamdeh, Numerical simulation and sensitivity analysis of effective parameters on heat transfer and homogeneity of Al_2O_3 nanofluid in a channel using DPM and RSM, Adv. Powder Technol. 27 (5) (2016) 1980–1991.
[27] K. Milani Shirvan, R. Ellahi, S. Mirzakhanlari, M. Mamourian, Enhancement of heat transfer and heat exchanger effectiveness in a double pipe heat exchanger filled with porous media: numerical simulation and sensitivity analysis of turbulent fluid flow, Appl. Therm. Eng. 109 (Part A) (2016) 761–774.
[28] M. Mamourian, K. Milani Shirvan, I. Pop, Sensitivity analysis for MHD effects and inclination angles on natural convection heat transfer and entropy generation of Al_2O_3-water nanofluid in square cavity by response surface methodology, Int. Commun. Heat Mass Transfer 79 (2016) 46–57.
[29] M. Mamourian, K. Milani Shirvan, S. Mirzakhanlari, A.B. Rahimi, Vortex generators position effect on heat transfer and nanofluid homogeneity: A numerical investigation and sensitivity analysis, Appl. Therm. Eng. 107 (2016) 1233–1247.
[30] M. Mamourian, K. Milani Shirvan, S. Mirzakhanlari, Two phase simulation and sensitivity analysis of effective parameters on turbulent combined heat transfer and pressure drop in a solar heat exchanger filled with nanofluid by response surface methodology, Energy 109 (2016) 49–61.
[31] K. Milani Shirvan, R. Ellahi, M. Mamourian, M. Moghiman, Effects of wavy surface characteristics on natural convection heat transfer in a cosine corrugated square cavity filled with nanofluid, Int. J. Heat Mass Transfer 107 (2017) 1110–1118.
[32] K. Milani Shirvan, S. Mirzakhanlari, M. Mamourian, N. Abu-Hamdeh, Numerical investigation and sensitivity analysis of effective parameters to obtain potential maximum power output: a case study on Zanjan prototype solar chimney power plant, Energy Convers. Manage. 136 (2017) 350–360.
[33] K. Milani Shirvan, M. Mamourian, S. Mirzakhanlari, R. Ellahi, Numerical investigation of heat exchanger effectiveness in a double pipe heat exchanger filled with nanofluid: a sensitivity analysis by response surface methodology, Powder Technol. 313 (2017) 99–111.
[34] K.M. Shirvan, S. Mirzakhanlari, A.J. Chamkha, M. Mamourian, Numerical simulation and sensitivity analysis of effective parameters on natural convection and entropy generation in a wavy surface cavity filled with a nanofluid using RSM, Numer. Heat Transfer, Part A: Appl. 70 (10) (2016) 1157–1177.
[35] K. Milani Shirvan, M. Mamourian, S. Mirzakhanlari, R. Ellahi, Two phase simulation and sensitivity analysis of effective parameters on combined heat transfer and pressure drop in a solar heat exchanger filled with nanofluid by RSM, J. Mol. Liq. 220 (2016) 888–901.
[36] ANSYS FLUENT CFD 15.0, the User's Guide, 2014.
[37] R. Shah, A. London, Laminar Flow Forced Convection in Ducts, Academic Press, New York, 1978.
[38] D.C. Montgomery, Design and Analysis of Experiments, John Wiley & Sons, 2008.
[39] G.E. Box, K. Wilson, On the experimental attainment of optimum conditions, in: Breakthroughs in Statistics, Springer, 1992, pp. 270–310.
[40] D. Freedman, R. Pisani, R. Purves, Statistics (International Student Edition), WW Norton & Co, 2007.
[41] A. Saltelli, M. Ratto, T. Andres, F. Campolongo, J. Cariboni, D. Gatelli, M. Saisana, S. Tarantola, Global Sensitivity Analysis: The Primer, John Wiley & Sons, 2008.